Chapter 3 : Experimentation and Methodology

The welding of titanium alloys is always very challenging due to their high affinity for atmospheric contamination. Welding becomes more challenging when it comes to welding dissimilar titanium alloys due to differences in their thermal conductivity, melting point, and elemental composition. In this chapter, the detailed procedure from the selection of the base materials (commercially pure titanium (CP-Ti) and Ti-6Al-4V alloy) to the preparation and characterization of dissimilar titanium alloy welds has been discussed in detail. The direct current (DC) pulsed gas tungsten arc welding (p-GTAW) process was utilized for producing dissimilar welds. A shielding setup has been designed and developed to protect the titanium alloy welds from atmospheric contamination. The experiments were performed in automated mode, where the welding torch was held on the overarm attached to a servo-controlled trolley to maintain constant speed. The other precautions, including electrode preparation, selection of shielding gas, and cleaning of the base plate, are taken into consideration for obtaining defect-free titanium welds. To minimize the number of variable parameters, several trials were conducted to fix the less impactful parameters for titanium welding. The dissimilar titanium (CP-Ti/Ti-6Al-4V) alloy welds were prepared at optimized pulsed parameters at different frequencies. Initially, a qualitative, non-destructive X-ray radiography test was performed on each weld. The radiographic quality welds were produced utilizing a shielding setup assembled with p-GTAW. The various characterization tools, like an optical microscope, stereo microscope, X-ray fluorescence, microhardness, X-ray diffraction, scanning electron microscopy, energy dispersive spectroscopy, tensile

testing, impact testing and impression creep testing were utilized to characterize the welds.

Table 3.1 Elemental composition (wt. %) of CP-Ti and Ti-6Al-4V

	Ti	Al	V	Fe	C
CP-Ti	Balance	-	-	0.21	0.04
Ti-6Al-4V	Balance	5.85	3.91	0.20	0.05

3.1 Material selection:

In this experimental work, 2 mm-thick CP-Ti and Ti-6Al-4V sheets were taken in the received condition. Titanium is one of the white metals where its alloys vary little with their contrast. Figure 3.1 shows the coupons of CP-Ti and Ti-6Al-4V, where no noticeable contrast variation could be observed. These coupons were cut into 100×50×2 mm^3 dimensions, and the edges were deburred, and surfaces were mechanically cleaned using a stainless-steel brush followed by acetone cleaning. The elemental compositions (wt.%) of materials are listed in Table 3.1. CP-Ti and Ti-6Al-4V are two widely utilized titanium alloys, each offering distinct advantages in various engineering applications. CP-Ti possesses nearly 99.5% pure titanium, boasts exceptional corrosion resistance, excellent formability, good impact toughness, good stress corrosion cracking, and is cheaper than other titanium alloys. These properties make it a preferred choice in industries such as aerospace, medicine, and chemical processing. On the other hand, Ti-6Al-4V, an alloy with added aluminium and vanadium, exhibits a combination of excellent strength, good corrosion resistance and reduced toughness and formability. Ti-6Al-4V finds extensive use in aerospace components, automotive parts, and medical implants. The balance between strength, corrosion resistance, and low density in both CP-Ti and Ti-6Al-4V makes them versatile materials for applications where durability, reliability, and weight considerations are critical. These two alloys, when used together, can provide the

advantages of both high strength and formability. Therefore, the investigation of dissimilar welding of CP-Ti to Ti-6Al-4V is vital to meet various industrial requirements.

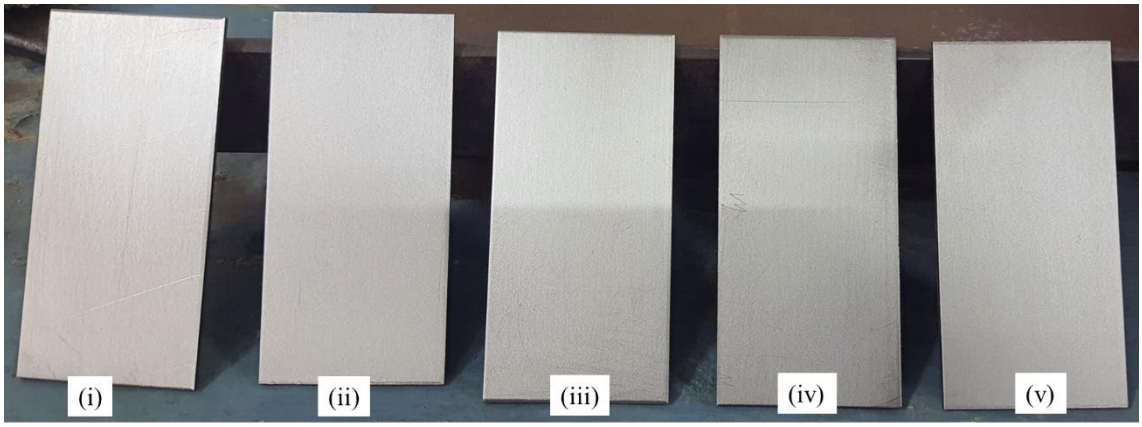

Figure 3.1 Base materials coupons of 100 mm×50 mm: (i), (ii) and (iii) CP-Ti; (iv) and (v) Ti-6Al-4V

3.2 Welding setup:

Figure 3.2 shows the complete welding arrangement for welding titanium alloys. Figure 3.2 (a) shows the indigenously designed and developed shielding setup attached to the servo-controlled Ador automatic welding trolley and the enlarged shielding setup inset. Figure 3.2 (b) shows the complete welding setup, which includes the GTAW power source, argon gas cylinder, argon gas flow meter or regulator, shielding setup and trolley. The welding was performed using an AC/DC water-cooled Lincoln Aspect^{TM} 300 gas tungsten arc welding machine. The shielding setup is assembled with an automatic welding trolley for maintaining constant speed and protecting the weldment from atmospheric contamination during welding. This automation was done by assembling a welding torch with a shielding setup and connecting it with a welding trolly using an arm. The pure argon (99.99%) gas was used as the shielding gas during the experiments. Argon, being non-reactive and heavier than atmospheric gases, can effectively replace them and provide better

shielding during the welding of titanium alloys. The flow rate required during welding was maintained using a gas flow controller. Arc was controlled using a foot paddle to avoid any disturbances in the welding arrangement. The gas lens was utilized over the basic diffuser to ensure laminar flow of shielding gas over the arc and the sheets to be welded. The laminar flow of shielding gas produces arc stability and better weldment shielding during welding. The large diameter ceramic cup compatible with gas was used to cover more shielding area during welding.

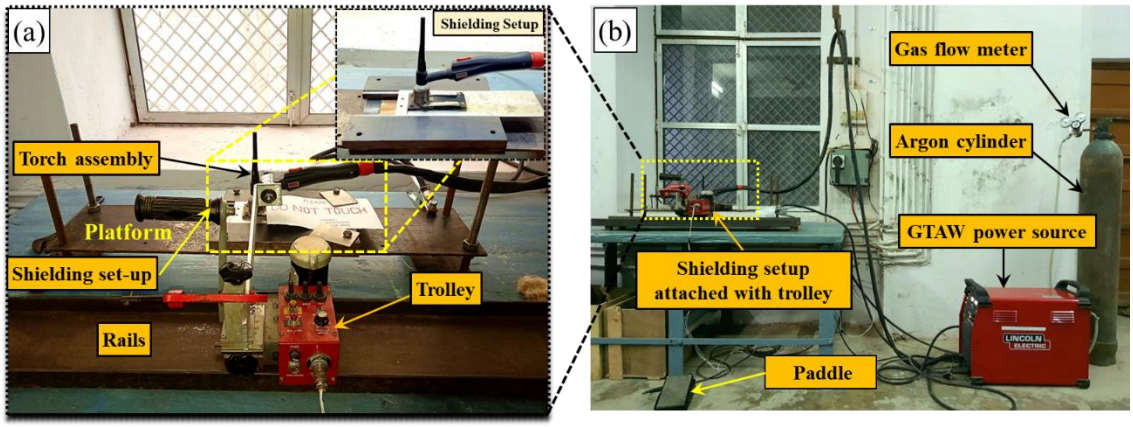

Figure 3.2 Experimental p-GTAW welding set-up highlighting shielding set-up in inset

3.2.1 GTAW power source

The Lincoln Aspect^{TM} 300 welding power source is a cutting-edge solution designed by Lincoln Electric to meet the demands of modern welding applications. It is designed in compliance with EN 60974-10:2014 AC/DC TIG water-cooled welding machine with an output welding current range of 2-300 A and an open circuit voltage (OCV) of 90 V DC was used for dissimilar welding of these alloys. It offers many advanced features and robust performance. This welding power source is engineered to deliver precision and efficiency in various welding processes, like gas tungsten arc welding (GTAW) and shielded metal arc welding (SMAW). Figure 3.3 (a-c) shows the Lincoln Aspect^{TM} 300 GTAW power source, enlarged front panel indicators, and controls and sequencer functions for setting welding parameters, respectively. First,

with the help of the control panel, a few basic settings, like current polarity and the arc initiation method, need to be selected. In this experimental work, direct current (DC) polarity and a high-frequency method for arc initiation have been selected. Thereafter, with the help of the sequencer function, the other welding parameters like current type (straight or pulled), gas pre-flow time, starting current percentage, start slope, operating amperage, end slope, finishing current percentage and gas post flow time need to be set. The experimental work has been carried out using pulsed current, but for comparison, straight current is also used. For utilizing pulse current during welding, there are a few more parameters, like peak current (operating amperage), percent of the total time of the pulse for peak current, pulse frequency (pulses per second) and background current (percentage of peak current). The use of sequencer functions and other important functions used for the operation of p-GTAW has been mentioned in Table 3.2. For more details about the specifications of the machine, refer to the user manual for this machine [112]. The effects of welding and pulse parameters were precisely observed and optimized for the final experimentation.

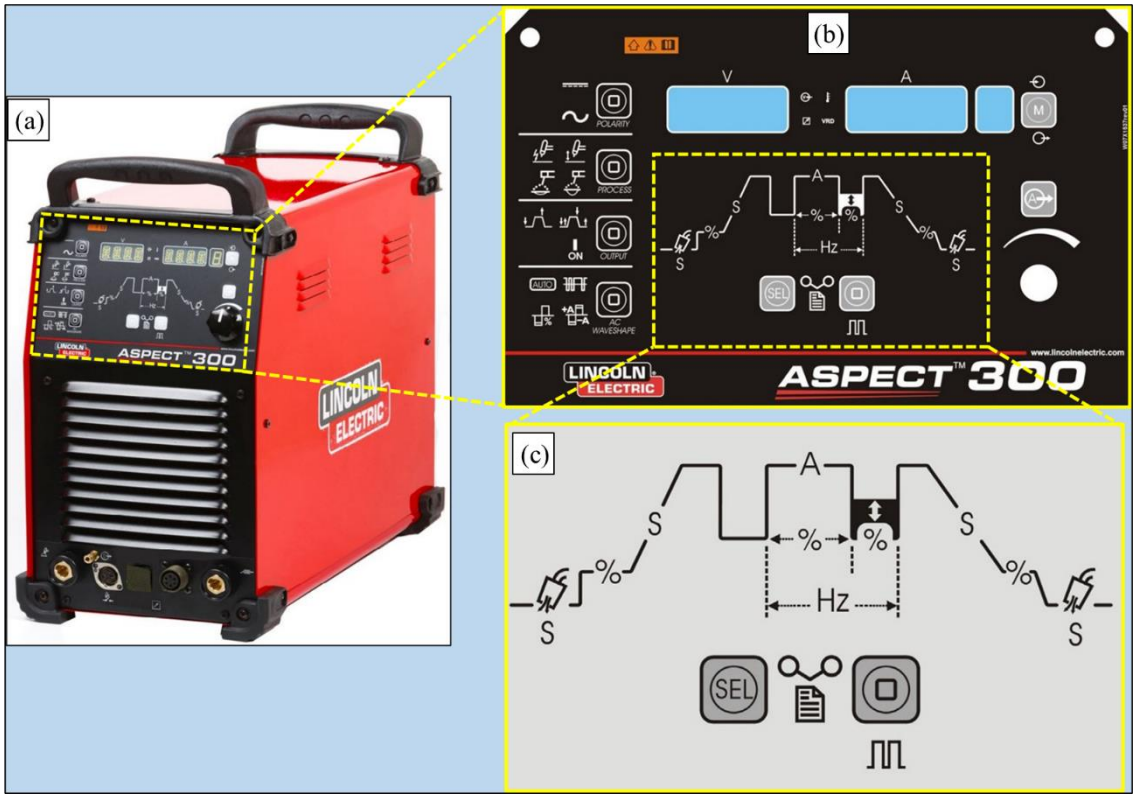

Figure 3.3 (a) GTAW power source; (b) front panel indicators and controls; (c) sequencer functions [112]

Table 3.2 Sequencer functions and other important functions used for operation of p-GTAW [112]

S.N.	Symbol on panel	Function of the symbol
1	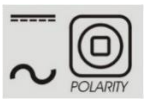	This icon is designated to **set the polarity** of the process in use: DC+, DC- and AC GTAW operations.
2		**Select the arc initiation mode:** 1. High-frequency mode 2. Touch and lift-Start
3		**Set the gas pre flow time:** Sets the time in seconds gas will flow prior to arc-start initiation
4		**Set the starting current percentage:** Sets the starting amperage for the process.

5		**Set the start slope:** Sets the time in seconds it takes the starting current to reach normal operating amperage.
6		**Set operating amperage:** Sets the amperage for all welding process permitted.
7		**Set the end slope:** Sets the time in seconds it takes the operating amperage to ramp down to the finishing current.
8	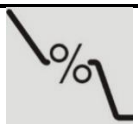	**Set the finishing current percentage:** Sets the finishing amperage percentage for the process.
9		**Set the gas post flow time:** Sets the time in seconds gas will flow after the arc is terminated.
10	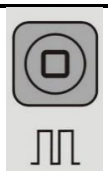	**Select the current type:** Pulse (ON/OFF) switch
11		**Set the percentage of the total time of pulse cycle for peak current.**
12		Set the pulse frequency (number of pulses-per-second)
13	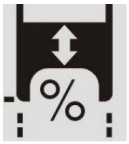	**Set the background current:** Background amperage is set as a percentage of the peak current.

3.2.2 Electrode selection and preparation:

The commonly used 2% thoriated tungsten electrode (contains 2% thorium oxide (ThO_2) by weight) was used for the p-GTAW of titanium alloys. The addition of thorium to the tungsten improves arc initiation and maintenance due to improvements in electron emission characteristics. For all the experimentation, a 2.4-

mm-diameter, 2% thoriated tungsten electrode was selected. The electrode with a diameter of 2.4 mm has a sufficiently high current-carrying capacity, and it could work perfectly well up to 200 A. The current value throughout the experimentation has not crossed the current level above 180 A.

A diamond grinding wheel was utilized for generating different tip angles on tungsten electrodes for p-GTAW. The rate at which spark is generated is directly proportional to the holding pressure. The uniform holding pressure was maintained while grinding the electrode tip angle for obtaining accurate tip angles, and it was precisely observed by the amount of spark generated and continuously rotating the electrode at a constant speed during grinding. The grinding wheel utilized for the generating electrode tip angles for GTAW was independently used to avoid any elemental contamination. Due to the presence of radioactive active elements, safety measures are essential during the grinding of tungsten electrodes [14, 19]. Along with the elemental contamination, the ground marks appearing on the tapered region also alter the weld bead appearance, penetration, and arc stability during welding [14]. Therefore, during the grinding of the electrode tip, the grinding direction and other precautions should be taken.

3.2.2.1 Effect of grinding direction on the weld beads:

Electrode preparation has a very vital role in the p-GTAW process. During the preparation of electrodes, the orientation of the electrode with respect to the grinding wheel is just as crucial as generating an accurate angle. The ground mark developed on the electrode tip alters the arc density and arc stability [19]. Figure 3.4 shows the grinding set-up and possible grinding directions, where Figure 3.4 (a, b) shows the grinding of the electrode in a perpendicular direction to the length and radial ground

marks appearing on the electrode tip, respectively. Figure 3.4 (c, d) shows the grinding of the electrode along the length and straight ground marks, respectively.

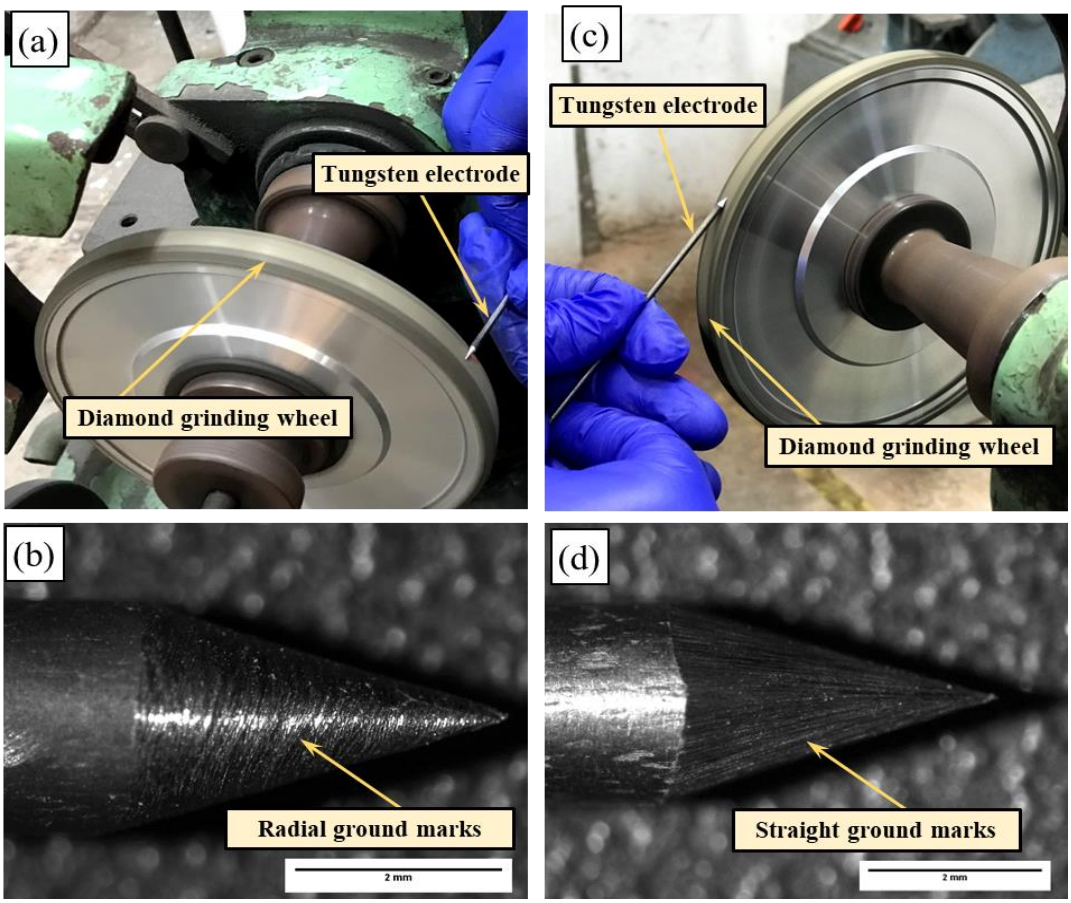

Figure 3.4 Effect of grinding direction on ground marks: (a) in the perpendicular to the length direction; (b) ground marks appeared in the radial direction; (c) along the length direction; (d) ground marks appeared along the length direction

The selection of the correct grinding direction is also very important for obtaining a sound weld, especially during the welding of titanium alloys, because most of the titanium alloys have applications in the aerospace and nuclear industries, where high precision welds are the utmost requirement. Therefore, the effect of these ground marks on weld appearance was observed, and Figure 3.5 shows the weld bead that appeared using the electrodes with radial and straight ground marks. Figure 3.5 (a) shows the weld bead prepared using an electrode with radial ground marks in the tip region, where varied weld bead width was observed throughout the weld. This varied

weld bead width was observed due to the presence of multiple cathode points and a wandered arc during welding [14, 19]. These radial ground marks disturbed the arc stability, which affected the weld bead appearance and altered the weld penetration at different locations. Figure 3.5 (b) shows the weld bead prepared using an electrode with straight ground marks in the tip region. The weld bead appeared using a straight ground-mark electrode and had constant bead width and penetration throughout the weld. The straight ground marks at the electrode tip aided in constricting and stabilizing the arc by guiding the electric current lines. Hence, the electrode must be ground in the direction of length to obtain a uniform weld bead.

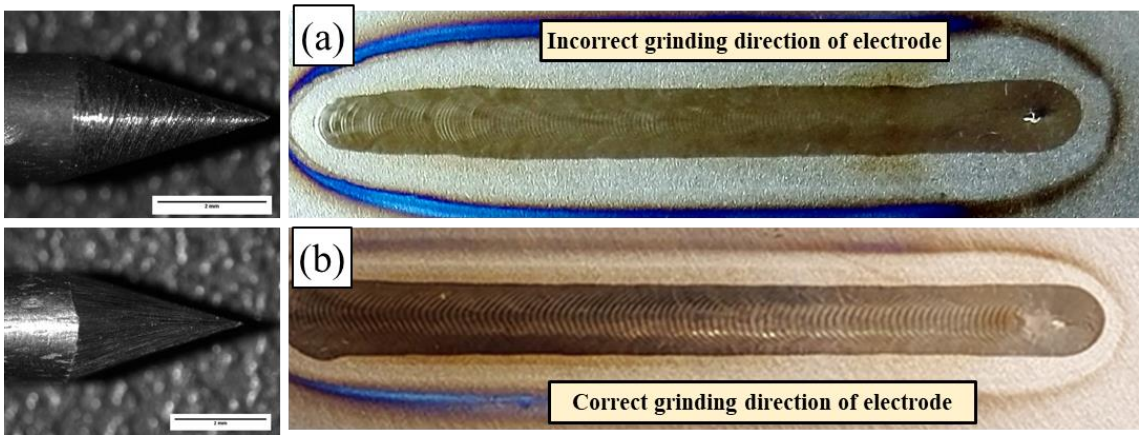

Figure 3.5 Weld bead appeared using different grinding direction electrode: (a) in the perpendicular to the length direction; (b) along the length direction

3.2.2.2 Preparation of different electrode tip angle:

Along with the effect of the grinding direction, the tip angle of the electrode also plays a very crucial role in developing the different weld geometrical elements. Here, the electrode tips are grounded to generate the different tip angles by grinding the electrodes in the direction of length. Figure 3.6 (a) shows the electrodes of 30°, 45°, 60°, 75°, and 90° tip angles, and Figure 3.6 (b) shows the measurement sample of the 60° electrode tip angle. All of the electrode tips were perfectly conical in shape, and the angles of the electrodes were determined by considering the electrode tip as a

right circular cone. The cone angles were measured using a toolmaker microscope and subsequently validated using the 'Image J' software. The tip angles closely matched (tolerance ±1) the intended values for which they were generated. The electrode tip was truncated with a diameter of around 0.3 mm for obtaining a stable and focused arc [14]. The electrode tip used for experimentation was not perfectly conical but a truncated cone. Truncated cone-shaped electrode tips not only provide a stable and focused arc but also help in improving the electrode life. The effect of electrode tip angle on weld bead geometry was studied using the electrodes below with varying tip angles.

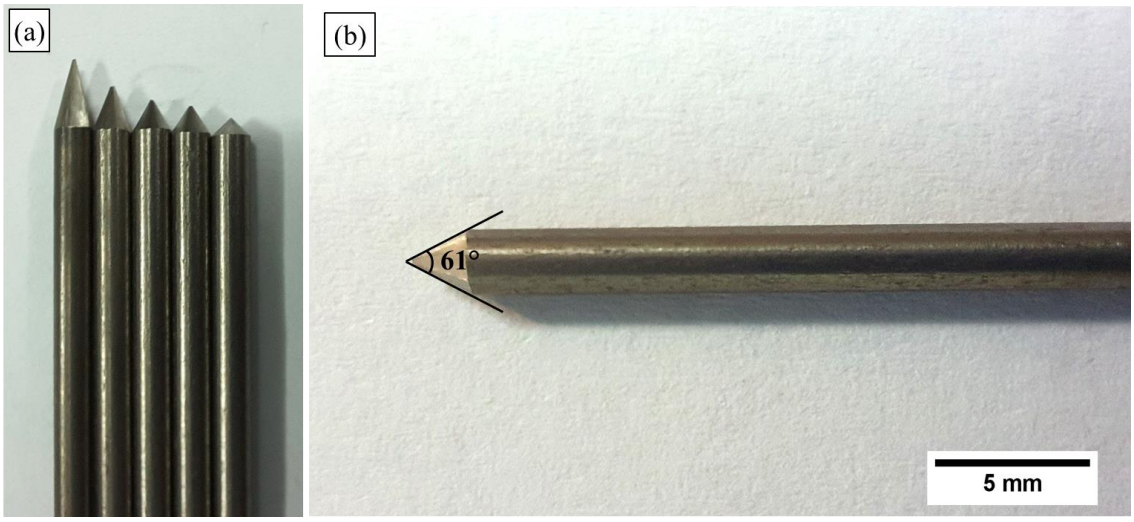

Figure 3.6 (a) Electrodes with 30°, 45°, 60°, 75°, 90° tip angles: (b) measurement of 60° electrode tip angle using 'Image J' software

3.3 Effect of standoff distance

Standoff distance refers to the distance between the non-consumable tungsten electrode and the workpiece. In some places, it is also known as an electrode gap or an electrode workpiece gap. In the GTAW process, the standoff distance should be as low as possible to avoid arc flaring and bring the maximum temperature of the arc point closer to the workpiece to obtain deeper penetration and increase the efficiency of the process. Several bead-on-plate (BOP) trials were conducted, and it was also

obtained from the literature that it should fall in the range of 3 mm to 1 mm [14]. Figure 3.7 shows the weld bead trials at a 2 mm to 1.2 mm standoff distance with an interval of 0.2 mm. These trials were performed on 2 mm CP-Ti sheets at 100 A constant current (conventional GTAW), 250 mm/min speed, and 10.5-11 V voltage. It could be observed from the weld beads in Figure 3.7 that, on decreasing the standoff distance from 2 mm to 1.6 mm, the weld bead width constricted and deeper penetration was observed. However, on further decrease in standoff distance from 1.6 mm, there was an insignificant effect on weld bead constriction and weld penetration, and non-uniformity in the weld bead was observed at 1.2 mm standoff distance. The changes in tungsten contamination and unstable arc also increase with a further decrease in the gap from 1.2 mm. From the above observation, it could be observed that the optimum value of standoff distance falls in the range of 1.6 mm to 1.4 mm. For safety, a 1.5-mm standoff distance was selected for further experimentation.

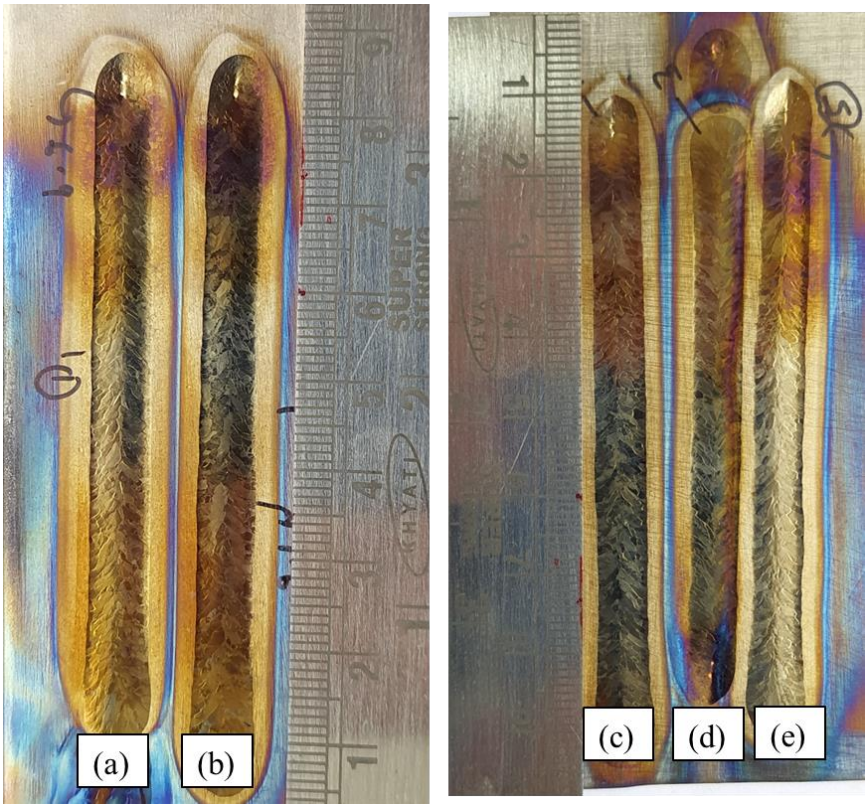

Figure 3.7 Weld bead at different stand-off distance at: (a) 2mm; (b) 1.8 mm; (c) 1.6 mm; (d) 1.4 mm; (e) 1.2 mm

3.4 Effect of variation of pulse frequency

The pulse frequency during p-GTAW plays a very important role in developing the weld bead profile. The Lincoln Aspect^{TM} 300 power source used for the experimentation could be utilized for pulse frequencies ranging from 0-2000 Hz. But after performing tests and critically analysing the literature, it was found that the low-frequency range is more useful. The large undercut and unstable arc was observed at frequencies above 12 Hz and at very high frequencies above 500 Hz [73]. The effect of frequency was insignificant, but disturbance in the arc was observed due to current pulsing. Hence, a few BOP trials were conducted at certain steps of frequency to observe the effect of variation in frequency on weld bead appearance. Figure 3.8 shows the weld beads at 2 Hz, 3 Hz, 4 Hz, 6 Hz, 9 Hz, and 12 Hz frequency and other key parameters listed in Table 3.3 are kept constant in each experiment.

Table 3.3 List of key parameters used for BOP welding at different frequency

Parameters	**Value**
Shielding Gas	Ar
Peak current (I_p) amp	143
Background current (I_b)/ Peak current (I_p)	1/2
Background current time (T_b)/ Peak current time (T_p)	1/2
Pulsed frequency (f) Hz	2, 3, 4, 6, 9, 12 Hz
Welding speed mm/min	250
Voltage (V) volt	10.5
Pre-flow time (Shielding gas) sec	1.5
Post-flow time (Shielding gas) sec	2.5
Electrode diameter (Thoriated 2%) mm	2.4
Electrode tip angle (degree)	60^o
Gas flow rate (l/min)	18

It is clear from the trial experiments that ripples have appeared in weld bead that were absent in the case of conventional or constant current GTAW (refer to Figure 3.7) due to the intermittent solidification in pulsed current GTAW, and these ripples have gotten finer as the frequency increased. Along with the effect on ripples, pulse frequency also affected the weld bead's appearance and penetration. The increase in pulse frequency led to a decrease in weld bead width and an increase in weld penetration. On increasing frequency, the intermittent time for background current or solidification became short; hence, the effect of high peak current predominated and constricted weld bead with deeper penetration was observed without burn-through. The high peak current in p-GTAW helps in obtaining deeper penetration, and the background current saves the weldment from burn-through by intermittent solidification in the weld. But at the same time, as the frequency increased, large undercuts and humps at the weld center were observed. The hump at the weld center and valley at the weld boundary was observed due to the increase in arc pressure with increasing frequency. The weld beads were almost flat up to 4 Hz, and hump and undercut started appearing at 6 Hz. Hence, all the experimentation was

performed between 3 Hz and 5 Hz.

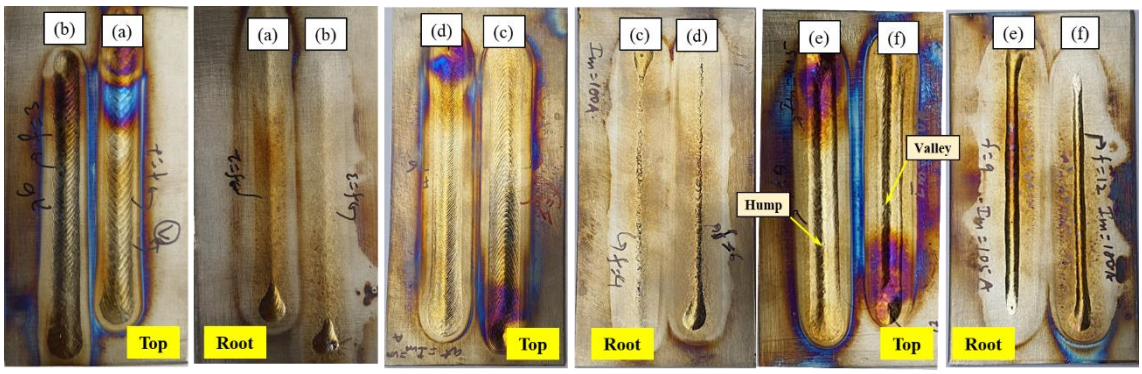

Figure 3.8 Top and root of weld bead prepared at different frequencies: (a) at 2 Hz; (b) at 3 Hz; (c) at 4Hz; (d) at 6Hz; (e) at 9Hz; (f) 12 Hz

3.5 Shielding gas quality test

Argon gas was selected for performing all the experiments related to the welding of titanium. Very high-purity (99.99%) argon gas is needed for welding titanium alloys. To ensure the quality of the agon gas, a spot test was conducted, in which a weld spot was created using a high flow rate of shielding gas (18 l/min) and utilizing sufficient pre-flow (for 15 s) and post-flow (for 20 s). The pre-flow time was selected depending on whether the shielding gas could replace the atmospheric gases, and the post-flow time was selected such that the temperature of the weld part reached below 350 °C. So, in the developed weld spot, only the effect of shielding gas will be observed. Figure 3.9 shows the weld spot of around 6 mm was created using high-purity argon (99.99%) shielding gas. The weld spot appeared silvery bright, and no colour appeared in the weld region as well as in the surrounding weld. The silvery brightness of the titanium weld certifies that the purity of the shielding is good and could be utilized for the welding of titanium alloys. The same purity of argon gas was utilized for performing all the experiments in the study.

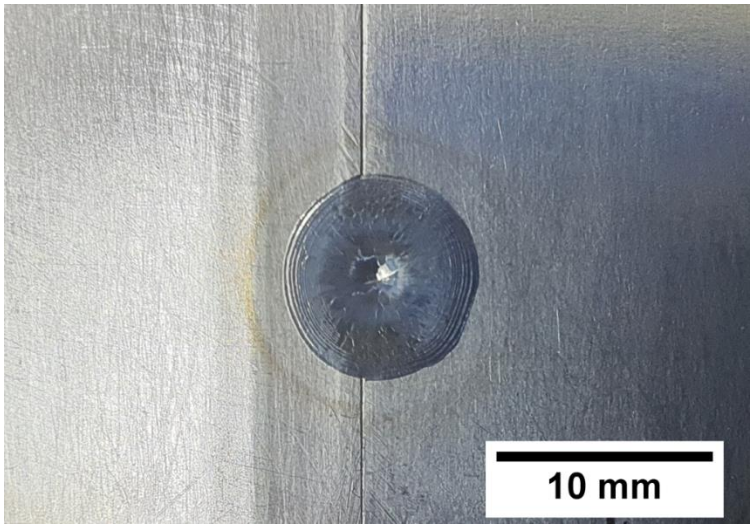

Figure 3.9 Weld spot created using argon as shielding gas

3.6 Development of shielding setup

Titanium alloys are susceptible to atmospheric contamination during welding. Hence, effective shielding is essential while welding of these alloys to protect the weld pool and nearby regions from atmospheric contamination. A simply designed shielding set-up has been developed to fulfil the requirement of shielding from atmospheric contamination, where shielding provided using the ceramic nozzle of the GTAW torch (primary shielding) was enough to protect weldment from atmospheric contamination. Figure 3.10 shows the three-dimensional schematic of the developed shielding setup in different views. The shielding set-up comprises a fixture for retaining sheets of various sizes and thicknesses to be welded, as well as space provided for the movement of the torch. The supports and base of the shielding set-up were made up using thick plates of mild steel for better rigidity, and a thick copper plate containing a groove was fixed for backing purposes. Other movable parts, like the slider, torch-holding arm and torch holder, were made using aluminium for easy movement. One end of the set-up was kept closed while other end was kept open for verifying the positioning of the sheets, electrode tip location, electrode gap, and monitoring to arc during welding. The electrode gap was precisely

managed using a stand-distance adjuster. The ceramic nozzle was press-fitted into the stand of the distance adjuster, and a welding torch was fitted with the set-up using it. For the assembly of the shielding setup, refer to Figure 3.2, which shows the detailed assembly of the shielding setup with the servo-controlled trolley and power source. In Figure 3.10, the movement direction of the slider is illustrated to provide more clarity on the movement during welding. The shielding set-up successfully prevented the top and root sides of the weldment from atmospheric contamination without using any back purging or a trailing shield. Hence, no extra arrangement for shielding was added to the setup.

The shielding set-up was capable of temporarily collecting the shieling gas provided during primary shieling in the empty space provided for holding plates and facilitating the welding torch travel, i.e., the space between the backing plate and the slider. Even after the completion of welding, the temporarily accumulated gas aids in protecting the weldment during cooling. A servo-controlled trolley and overarm connecting shielding setup and trolley were used to automate the welding process. Automation in p-GTAW helps provide the best control over heat input and a smooth weld by fixing constant speed. This indigenously developed shielding setup offers several advantages over traditional methods used for welding titanium alloys. Superior quality titanium welds could be produced at a moderate gas flow rate (18 l/min) and without using any external shielding. The shielding setup considerably minimized the wastage of shielding gas and the time required for each run. The design of this shielding setup could be adapted and utilized for large-scale and on-site welding as well.

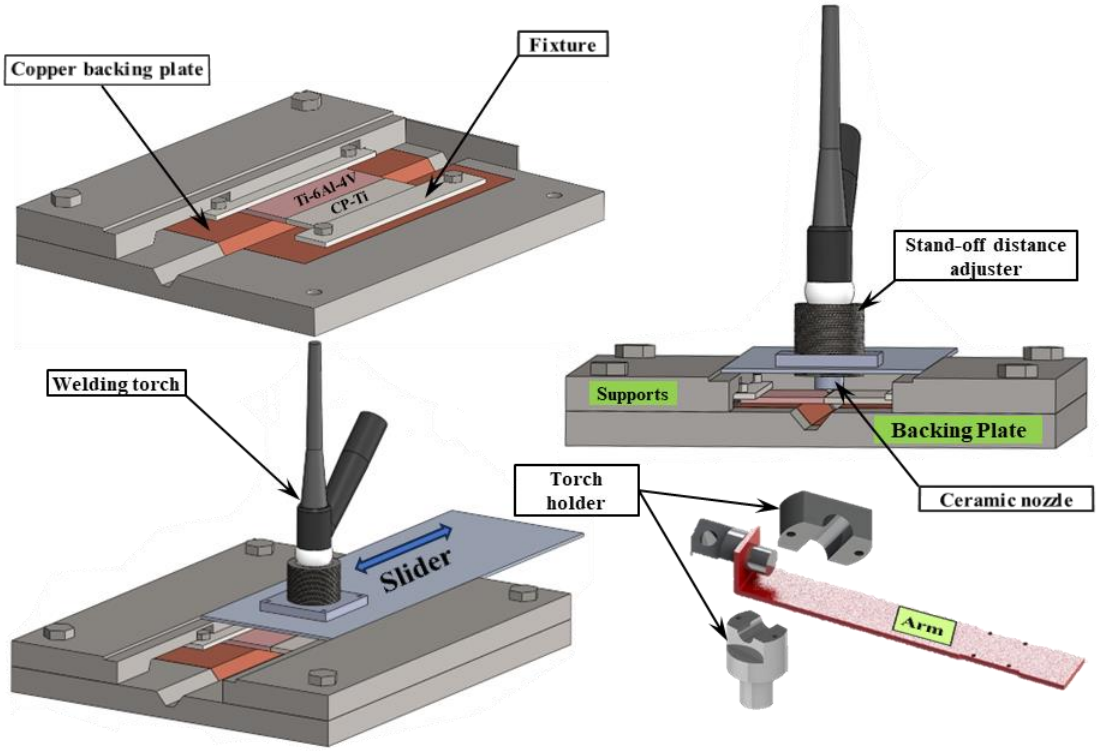

Figure 3.10 Three-dimensional schematic of developed shielding set-up

Figure 3.11 (a) shows the weld produced using conventional GTAW shielding without any arrangement of external shielding. The weld and nearby region got contaminated by atmospheric gases and formed a chalky white layer on the surface. The chalky white layer indicates that the contamination has reached the bulk and weld, which is not acceptable. Figure 3.11 (b) shows the weld bead produced at optimized shielding parameters using the developed shielding setup. Figure 3.11 (c-d) shows the X-ray diffraction analysis of dissimilar weld produced without using shielding-setup and with using shielding-setup.

The major peaks of the XRD pattern for the dissimilar weld produced without using a shielding setup confirmed the formation of oxide (TiO_2) in this region. No peak corresponding to any oxide of titanium was observed in the dissimilar weld produced using the shielding setup, confirming that the shielding setup successfully protected the weldment from atmospheric contamination. The welds produced using the shielding setup were having silvery-bright colour on the top and root sides of the

weld (refer to Table 3.4).

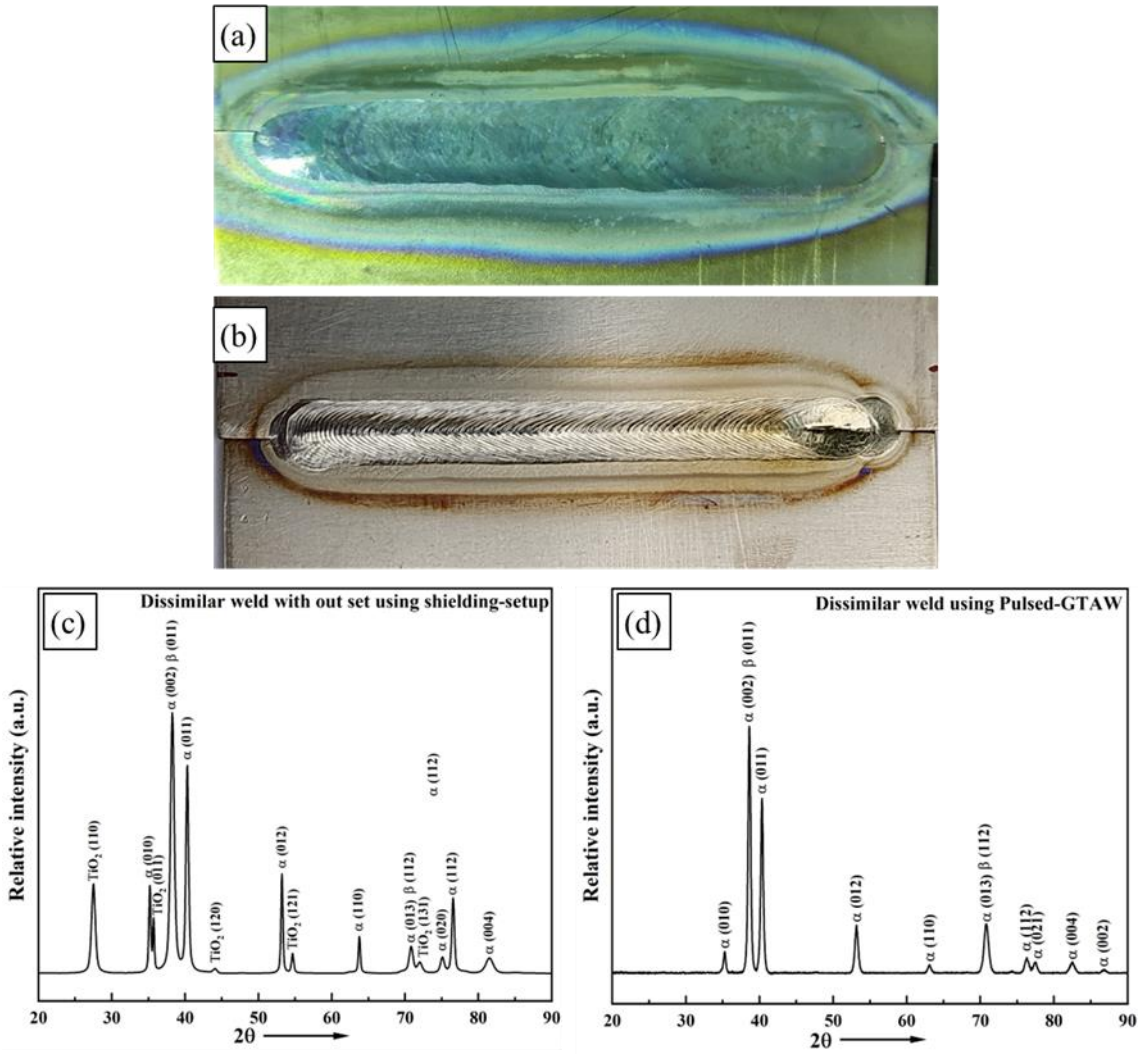

Figure 3.11 Weld bead prepared without and with using shielding setup on Ti-6Al-4V: (a) without using shielding setup; (b) with using welding setup; (c) X-ray diffraction analysis without shielding-setup; (d) X-ray diffraction analysis using shielding-setup

Independent utilization of shielding setups for welding of titanium alloys was not sufficient to obtain an atmospheric contamination-free titanium alloy weld because the weld region needed to be protected after completion of welding until the weld reached around 450 °C. Hence, along with the shieling setup, the advantages of pre-flow and post-flow were utilized, and their times were optimized so that the weldment obtained would be free from atmospheric contamination. Table 3.4 shows that the weld beads appeared at various pre-flow and post-flow times. The different

bead colors appeared at various gas flow rates and different pre-flow and post-flow times. Typically, the color variation during welding indicates different levels of contamination, which depends on the thickness of the oxide layer. For example, a chalky white color indicates severe contamination, while this contamination decreases through blue, straw, and finally, a silvery bright color, which is considered acceptable weld quality [22]. At 15 seconds of pre-flow and 20 seconds of post-flow and at an 18 l/min flow rate of shielding gas during welding, it helped in obtaining a silvery-bright, contamination-free weld bead. Where heavy inert argon gas replaced the lighter active atmospheric gases during the pre-flow and post-flow of shielding gas, it helped in maintaining the inert atmosphere after the completion of welding.

Table 3.4 Weld bead appearance at different flow rate and pre- and post-flow rates using setup

Weld bead appearance	Gas flow rate l/min	Pre flow (sec)	Post flow (sec)
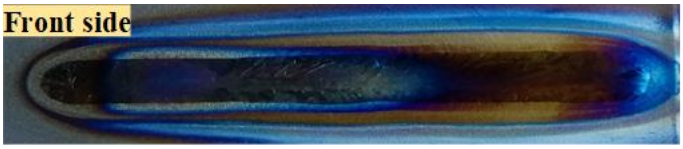	15	1.5 (default)	2 (default)
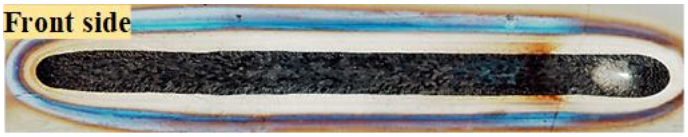	17	5	10
	18	10	15
	18	15	20
	18	15	20

3.7 Weld preparation

As discussed above, the major challenge during the welding of titanium alloys is protecting the weld pool and nearby regions from atmospheric contamination. The developed shielding setup worked well and helped in obtaining contamination-free welds. But there are some other challenges related to the p-GTAW of titanium alloys, like the cleaning of titanium alloy sheets before welding, edge preparation for butt welding, and optimization of the weld and pulse parameters for obtaining sound welds.

3.7.1 Cleaning and edge preparation

Cleaning titanium sheets before welding is a crucial step to ensure the success of the welding process and the quality of the final weld. Titanium alloys are known for their sensitivity to contamination, and any impurities on the surface can lead to poor weld integrity and performance. Hence, as-received sheets were cleaned in different steps before welding, square flat edges were prepared by milling the edges up to flat, and edges were deburred using a fine-grade file for butt welding of dissimilar titanium alloys. Figure 3.12 shows the as-received titanium sheets and various steps of cleaning and edge preparation. As-received sheets were first acid-pickled with 20 ml of HNO_3 and 5 ml of HF in 100 ml of water at room temperature for the removal of any kind of oil, grease, or dirt from the surface. After drying, these sheets were mechanically cleaned using a stainless-steel wire brush, followed by acetone cleaning for the removal of any acid strains from the surface. Cleaned and square-edged titanium alloy sheets were used for dissimilar titanium alloy welding.

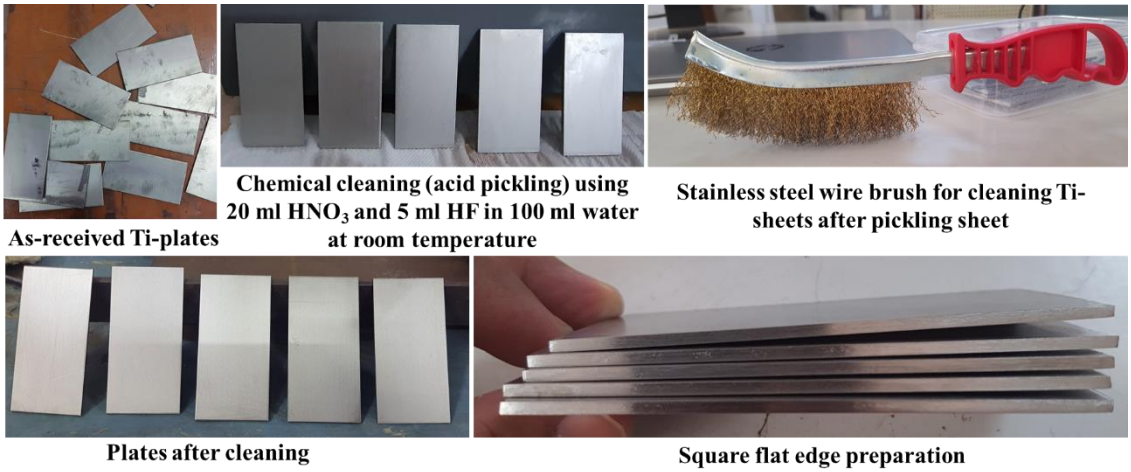

Figure 3.12 Different steps of cleaning and edge preparation of titanium sheets

3.7.2 Bead on plate welding trials

Before performing dissimilar titanium alloy welding, bead-on-plate (BOP) welding trial experiments were carried out on 2 mm-thick Ti-6Al-4V sheets to ensure full penetration and analyze the effect of current pulsing during welding. Figure 3.13 (a) shows the top and root of the weldment appeared using conventional current GTAW, and Figure 3.13 (b) shows the weldment appeared using pulsed current GTAW. These weld beads were prepared with nearly the same heat input; however, a narrower and steeper weld bead was observed in the case of p-GTAW. The detailed list of parameters used for conventional and pulsed GTAW is mentioned in Table 3.5 and Table 3.6.

Table 3.5 List of parameters used during conventional-GTAW

Parameters	Value
Shielding Gas	Ar
Welding current (I) amp	110
Welding speed (v) mm/min	250
Voltage (V) volt	11
Pre-flow time (Shielding gas) s	15
Post-flow time (Shielding gas) s	20
Electrode diameter (Thoriated 2%) mm	2.4
Electrode tip angle (degree)	60^o
Gas flow rate (l/min)	18

Table 3.6 List of parameters used during pulsed-GTAW

Parameters	**Value**
Shielding Gas	Ar
Peak current (I_p) amp	189
Background current (I_b)/ Peak current (I_p)	2/5
Background current time (T_b)/ Peak current time (T_p)	7/3
Pulsed frequency (f) Hz	5
Welding speed mm/min	250
Voltage (V) volt	11.5
Pre-flow time (Shielding gas) sec	15
Post-flow time (Shielding gas) sec	20
Electrode diameter (Thoriated 2%) mm	2.4
Electrode tip angle (degree)	60^o
Gas flow rate (l/min)	18

A silvery-bright colour appeared at the top and root sides of the weldment, which ensures the acceptable quality of the weld. The weld bead that appeared using constant current was flatter and smoother than the weld produced using pulsed current, but large axial grains were observed at the centre of the weld bead using constant current GTAW, which were absent in the case pulsed current GTAW. These large axial grains are detrimental because they often result in reduced mechanical properties such as strength, hardness, and toughness, which create anisotropy in the material. The weld bead appeared using pulsed current had clear ripples with little hump at the center. During p-GTAW, the current level changes from peak current (I_p) to background current (I_b) in a fixed internal, where melting occurs during peak current and solidification occurs during background current. Due to intermitent melting and solidification, fine grains and ripples appeared in the weld region. The high arc pressure was created due to the high peak current in p-GTAW, which led to the formation of a little hump in the weld center. Along with avove advantages of p-

GTAW over conventional GTAW, current pulsing during GTAW also produces constricted and deeper penatration.

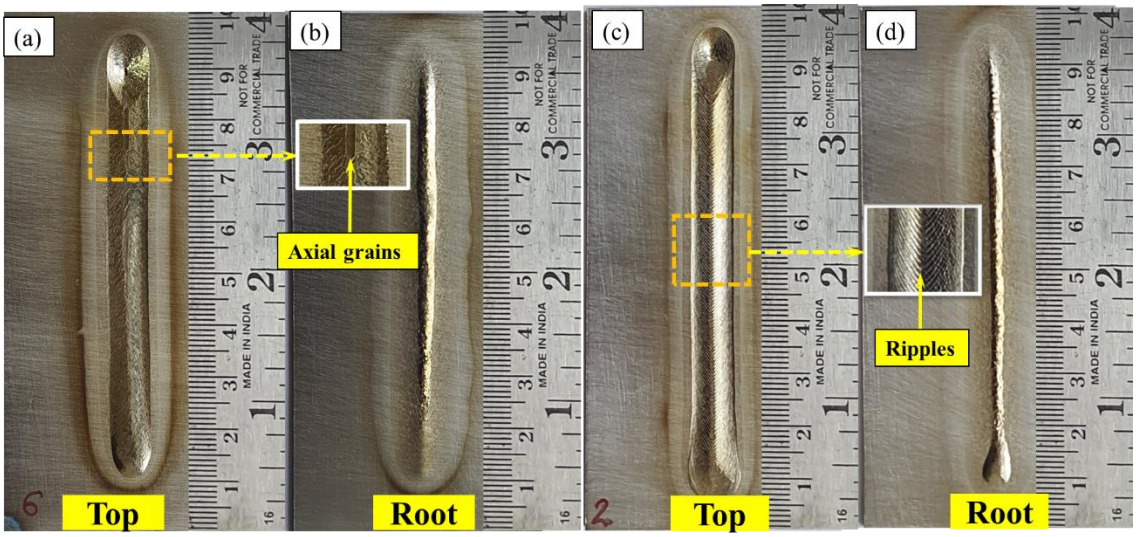

Figure 3.13 Bead on plate welding on Ti-6Al-4V: (a, b) top and root side of the weld prepared using conventional GTAW; (c, d) top and root side of the weld prepared using p-GTAW

3.7.3 Preparation of dissimilar weld

The dissimilar (Ti-6Al-4V/CP-Ti) titanium alloys welds were produced using conventional and pulsed-GTAW. Figure 3.14 (a-b) shows the top and root of dissimilar weld produced using conventional GTAW, and Figure 3.14 (c-d) shows the dissimilar weld produced using p-GTAW. The dissimilar welds were prepared at almost the same parameters listed in

Table 3.5 and Table 3.6 other than the pulse frequency. They were prepared at a 3 to 5 Hz pulse frequency with an interval of 0.5 Hz and have been analysed in the results and discussion chapter. Here also pulsed current welds were prepared at the same mean current used during constant conventional GTAW for keeping the same heat input in both types of welds. During dissimilar welding, sheets were firmly clamped and tacked before the welding run to avoid misalignment and reduce distortion in the weldment. Dissimilar titanium alloys also had a silvery-bright colour on either end, with a light straw colour away from the weld region. The straw colour that emerged

from the weld has no effect on the weld quality. The appearance after welding of titanium alloys ensures the acceptability of welds and is considered free from atmospheric contamination. As a result, on the basis of visual assessment and X-ray diffraction analysis (refer to Section 3.6) of the welds, it could be concluded that the shielding setup served its purpose and that the welds obtained were of acceptable quality.

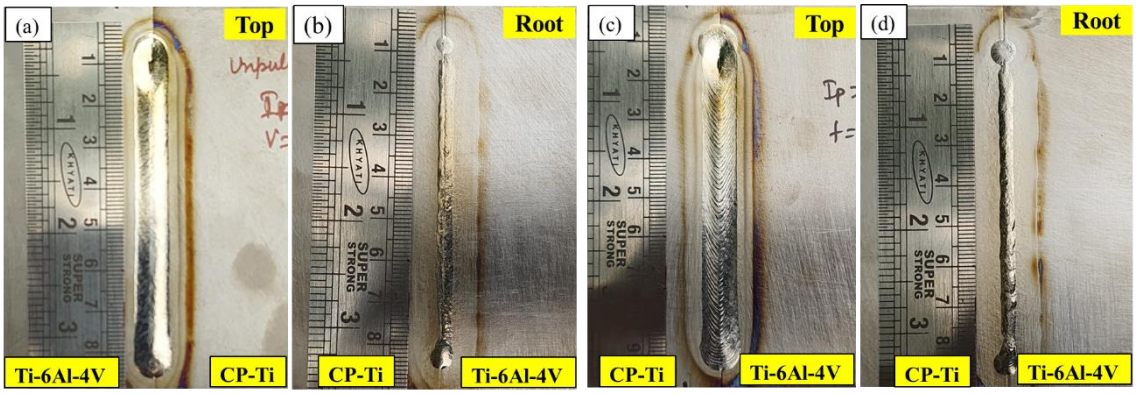

Figure 3.14 Dissimilar titanium alloys (Ti-6Al-4V/CP-Ti) welds: (a, b) top and root side of the weld prepared using conventional GTAW; (c, d) top and root side of the weld prepared using p-GTAW

3.8 Characterization of welds

Successfully welded defect-free specimens were utilized for X-ray radiography, metallographic studies, phase analysis, mechanical testing, and high-temperature creep analysis. The metallographic studies were carried out to analyze the macro- and microstructural changes that appeared after p-GTAW for BOP welding and dissimilar welding and compare them with conventional GTAW welds. The high-magnification microscopy and elemental analysis throughout the welds were carried out using high resolution scanning electron microscopy (SEM). The new phases that appeared on the surface as well as on the bulk after welding were analysed using X-ray diffraction analysis (XRD). Mechanical tests like tensile testing, the Charpy impact test, and hardness analysis of the weldments were performed to analyse the

weld strength and hardness of the different regions. The high temperature creep analysis of different zones of dissimilar weld was carried out using impression creep testing, where different zones of the weldment were independently controlled using this method, and steady state creep rate, activation energy, and stress exponent were determined.

3.8.1 X-ray radiography

X-ray radiography stands as a widely utilized non-destructive testing technique in the welding industry for assessing the quality of weld joints. This method employs X-rays to produce images revealing internal defects within the weld. Due to their small wavelength, X-rays possess exceptional penetrating capabilities, even in metals. Increasing the tube voltage and beam filtration further amplifies this penetrating capacity. As X-rays are irradiated on the welded plates, some X-rays are absorbed by the material, while the remainder passes through and is captured by the X-ray detector positioned behind the plate. The degree of X-ray absorption hinges on the density and crystal structure of the material, and the detector can be in the form of a photographic film or a modern digital detector.

When the plate exhibits discontinuities or contains foreign material at certain locations, variations in absorbed energy occur, which are depicted on the photographic film as shades of black and white. Consequently, all weld discontinuities become apparent on the X-ray film. A trained technician can interpret the type of defect and its location by looking at the shades of the film. However, the X-ray radiography technique is time-consuming, expansive, and has several health hazards. So, it is strongly recommended that well-trained operators conduct this testing.

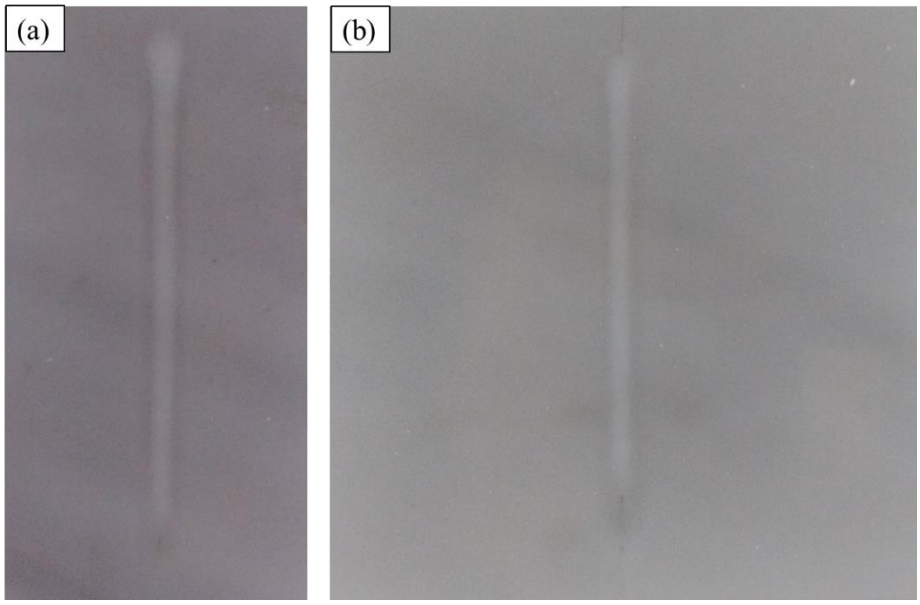

Figure 3.15 X-ray radio graphic film of: (a) BOP welding on Ti-6Al-4V using p-GTAW; (b) dissimilar titanium alloys (CP-Ti/Ti-6Al-4V) weld using p-GTAW

It is well understood that p-GTAW is a high-heat input fusion welding process and prone to some sub-surface flaws such as tungsten inclusion, porosity, and oxide trapping. Therefore, an X-ray radiography test becomes imperative for detecting these flaws potentially present within the weld metal. Figure 3.15 (a–b) shows the X-ray radiographic film of BOP welding on Ti-6Al-4V and dissimilar titanium welding using p-GTAW. X-ray radiography of the welds was carried out following the ASTM E1032 [113] standard using a Gamax Inc. industrial X-ray unit (Model: Classic 333) (focal spot: 1.5 mm). The X-ray radiographic films were acquired after an exposure time of 1.8 seconds. The radiographic standard welds were prepared, and they were free from any kind of inclusion or porosity.

3.8.2 Sample extraction location from welded plates

Figure 3.16 shows a schematic diagram of the locations of the different specimens extracted from the welded plates. ‘D’ represents the discarded material from both ends of the welded plates. Various specimens, such as metallographic samples for microstructural study (denoted by M) and hardness measurement sample (denoted by

H), full length standard transverse tensile testing (denoted by T_1), reduced section tensile testing (denoted by T_2), Charpy impact testing specimens notch in weld region (denoted by I_W) and notch in HAZ (denoted by I_H), and Impression creep testing specimens (denoted using C_I) were extracted from the dissimilar welded plates for characterization.

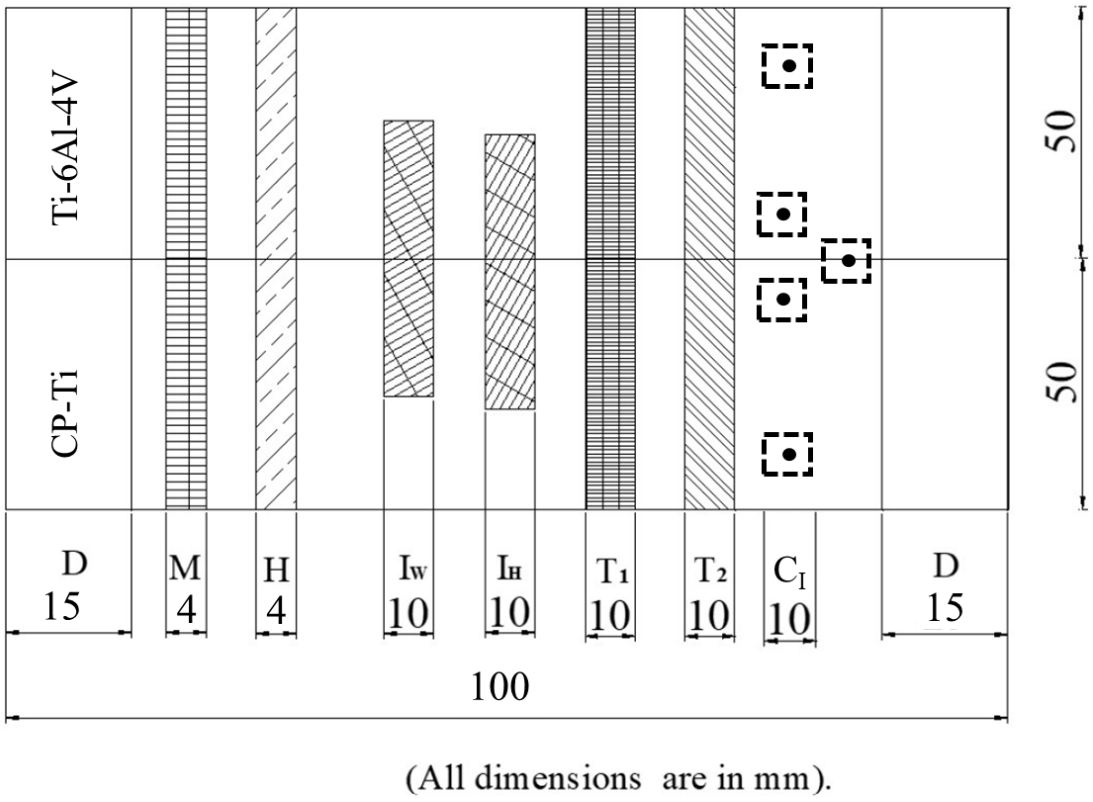

Figure 3.16 Schematic diagram of extraction of different specimens for characterizations from the welded plates

3.8.3 Metallography of welded specimens

Metallography plays a crucial role in the characterization section, allowing for the observation of metallurgical changes that have occurred in the transverse section of weld samples. The weld beads were cut cross-sectionally and hot-mounted using bakelite for sample preparation. Specimens were first polished using fine grades of emery paper up to 2500 grit size, followed by cloth polishing using 0.25 µm particle size of alumina suspension in water up to mirror finish. First, to understand the effect

of welding parameters on weld characteristics, mirror finish samples were macro-etched using concentrated etchant (15 % HNO3, 10% HF, and 75% distilled water) for 2 minutes at room temperature. Macro-etching of samples helped in highlighting the weld profile and differentiating all the regions (base, HAZ, and weld) of the weldment. Stereomicroscopy was performed at low magnification for analysing the weld bead profile. For optical microscopy, freshly mirror finish polished samples were etched for 30–40 s at room temperature (25 °C) using optimized Kroll's reagent (3% HNO3, 2% HF, and 95% distilled water). The micrographs differentiating different grains and morphologies were captured using a metallurgical optical microscope. The microscopy of the transverse section of specimens was carried out following the ASTM E407 standard [114].

3.8.3.1 Stereomicroscopy

Stereomicroscopy is a specialized optical microscopy technique designed for the low magnification observation of three-dimensional objects. Key features of a stereo microscope include a binocular eyepiece, which allows for comfortable and natural viewing with both eyes, providing depth perception. Stereo microscopes typically have a zoom capability, enabling users to adjust the magnification level as required. This versatility makes them suitable for various applications across fields such as biology, geology, electronics, and materials science. A stereo microscope is an invaluable tool for researchers, scientists, and technicians who require detailed visualization at low magnification. The Leica S9i stereo-microscope was utilized for analysing the weld bead profile and various weld geometrical elements. The low magnification feature of the stereomicroscope helped in capturing all the regions of the weld (base, HAZ, and weld) together at high resolution. The measurement of various geometrical elements was performed using ‘Image-J’ software.

3.8.3.2 Optical microscopy

Optical microscopy is a fundamental and versatile imaging technique that utilises visible light to magnify and visualise specimens at the microscale. The key components of an optical microscope include an illumination source, a condenser lens for focusing the light onto the specimen, objective lenses for magnification, and an eyepiece for observation. For performing microstructural characterization, a reflected-light metallurgical microscope is utilised, where opaque samples are illuminated using visible light, and the resulting reflected light is used in creating the image. These microscopes are equipped with high-magnification objective lenses, providing clear images. To examine microstructural changes post-welding, optical microscopy was conducted. Optical micrographs of different regions were captured at varying magnifications using an inverted Leica DFC295 metallurgical microscope. The effects of different welding parameters on grain size and various morphologies were analysed.

3.8.4 X-ray diffraction

X-ray diffraction is a powerful, non-destructive technique used to investigate the structure of crystalline materials. This technique could be used for liquids, powders, thin films, and crystals; hence, it is used in physics, chemistry, geology, and materials science. This technique is based on the scattering of X-rays from an ordered structure and constructive interference to form a diffraction pattern that can be analysed to determine the atomic and molecular structure of the material. Apart from atomic arrangement, it can also be used for determining the average grain size, lattice parameters, strain, preferred orientation, thermal expansion, and crystalline phases. Phase analysis of the base and welded specimens was carried out using the X-ray diffraction (XRD) technique to observe the effect of shielding setup and

welding. Samples were extracted from the as-received CP-Ti and Ti-6Al-4V and weld sections of welded specimens. XRD was performed on the 9kW Rigaku SmartLab X-ray diffractometer for the scan angle range of 20°–80°. For the phase determination, the observed XRD patterns were analysed using X'pert High Score Plus software and matched with references.

3.8.5 Microhardness testing

The hardness of a material refers to its resistance to plastic deformation, indentation, or scratching. Microhardness testing is a technique utilized to determine the hardness of materials at micron scales, particularly at the microstructural level. It plays a vital role in understanding the mechanical behaviour of materials at the microscopic level. It provides valuable insights into the mechanical properties, wear resistance, and overall durability of materials. Common microhardness testing methods include Vickers and Knoop hardness tests. The Vickers microhardness test involves using a pyramidal diamond indenter, while the Knoop test utilises a rhombic-shaped diamond indenter. Both methods provide a measure of the material's resistance to indentation.

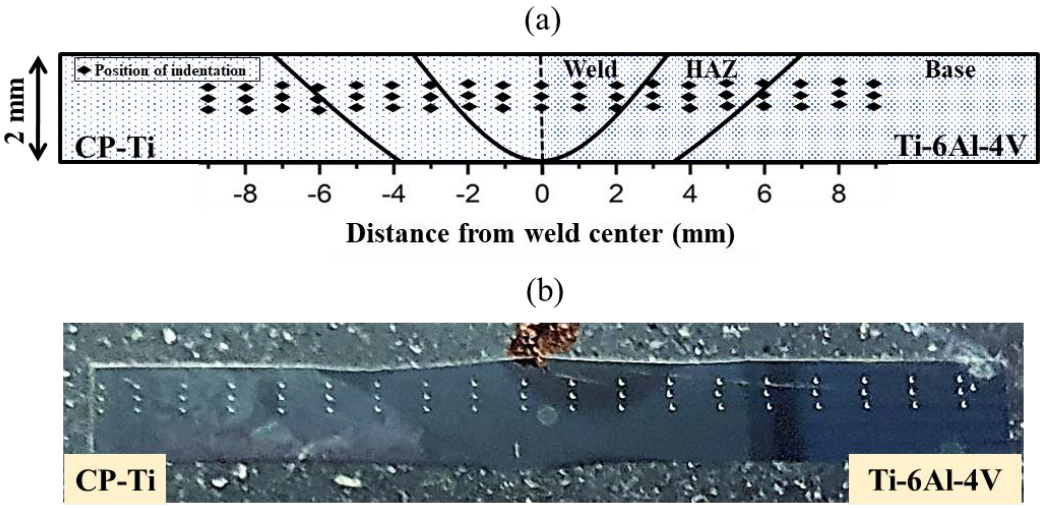

Figure 3.17 (a) Schematic of the indentations made with their locations; (b) transverse section of dissimilar titanium alloy (CP-Ti/Ti-Al-4V) weld with Vickers indentations

For the current study, a Vickers microhardness test was performed on the transverse section of welded specimens. The specimens for microhardness were prepared the same as the optical microscopy. Microhardness measurements were performed across the weldment. Figure 3.17 (a) shows the schematic of the indentations made with their locations on dissimilar titanium alloys (CP-Ti/Ti-6Al-4V) welds. Figure 3.17 (b) shows the actual indentation created after Vickers hardness test. Indentations for hardness measurement were taken at an interval of 1 mm, and three indentations were made at particular locations by moving the indenter in the thickness direction by 250 µm. Vickers hardness testing was carried out following ASTM-E92 on a semiautomatic microhardness tester, using a diamond pyramidal indenter at a load of 200 gf for a dwell time of 10 sec [115].

3.8.6 Scanning electron microscopy and EDS analysis

Scanning Electron Microscopy (SEM) is a powerful imaging technique used for high-resolution, three-dimensional imaging of surfaces at the micro- and nanoscale. Unlike traditional optical microscopes that use light, SEM employs a focused beam of electrons to achieve much higher resolution and depth of field. These electrons are accelerated using high voltage and focused using electromagnetic deflection coils, also known as condenser lenses. When an electron beam is scanned over a specimen, these electrons will have different interactions with the specimen. Depending on the interactions, these electrons will carry various information regarding the specimen. The information is collected by using various detectors installed in the machine, e.g., a backscattered electron (BE) detector, a secondary electron (SE) detector, and an energy dispersive X-ray spectroscopy (EDS) detector. The BE detector gives information regarding grain boundaries, domains and phases; the SE detector gives information regarding the surface morphology of the specimen; and the EDS detector

provides information regarding the elemental composition of a sample. SEM is considered an essential tool for researchers and scientists seeking detailed insights into the surface morphology and composition of materials.

In this study, a high-resolution FEI Nova Nano SEM 450 with the EDAX Pegasus system was utilised for capturing high-magnification micrographs, analysing fractured tensile and creep samples, and performing energy dispersive X-ray spectroscopy (EDS) of welded specimens at different locations.

3.8.7 Tensile testing

Tensile testing is a fundamental and widely used mechanical testing method to evaluate the mechanical properties of materials, especially metals, polymers, and composites. This test helps engineers and scientists understand how a material responds to uniaxial tensile loading. It provides very crucial information for design, quality control, and material selection in various industries such as aerospace, automotive, construction, and manufacturing. Tensile testing is well accepted for determining the strength and ductility of the welded joints. It provides the stress-stain diagram from which elastic deformation, yield/proof strength, ultimate tensile strength, and total deformation until fracture can be calculated.

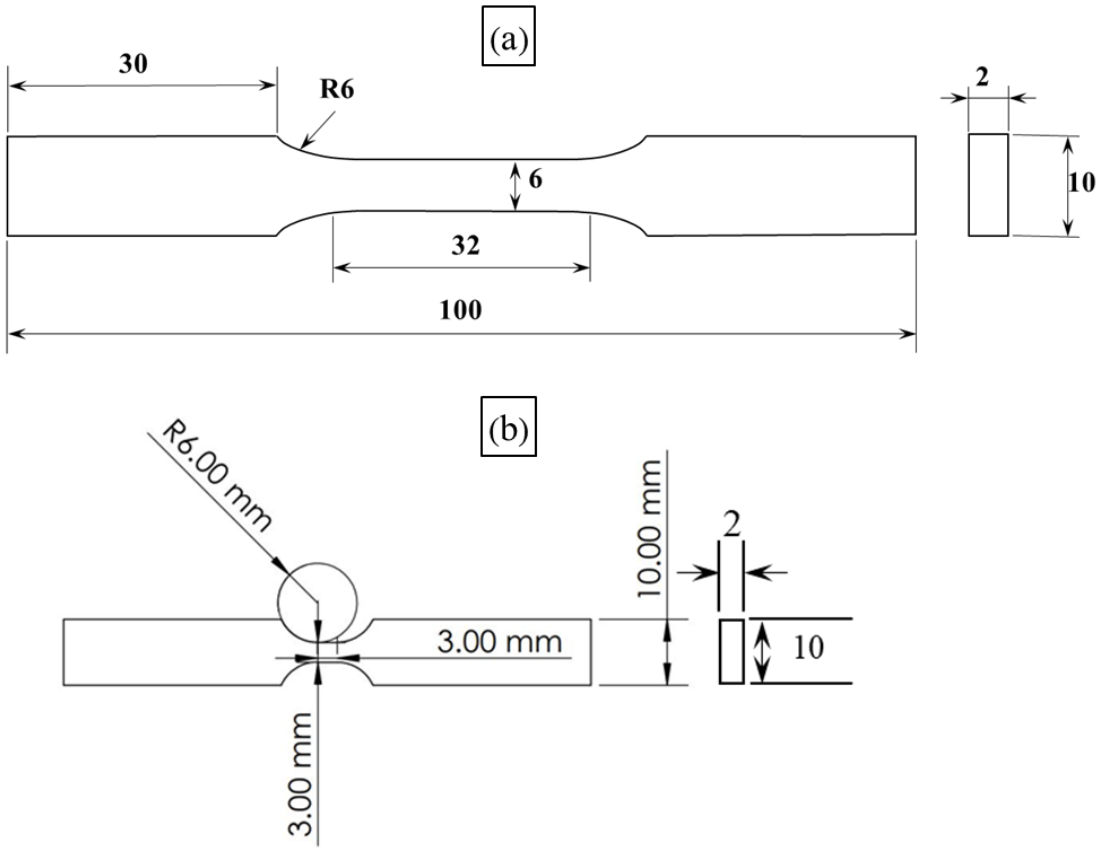

Figure 3.18 (a) Design of full-length tensile specimen with dimensions; (b) design of reduced-section tensile specimen with dimensions

Two types of tensile specimens were tested as per the ASTM E-8 (M) standard on a screw-driven 100 kN (Instron 8801) servo hydraulic universal testing machine system at room temperature. Figure 3.18 (a) shows the sub-size flat full-length transverse tensile specimen with 32 mm gauge length, 6 mm width in gauge length, and 2 mm thickness and Figure 3.18 (b) shows the sub-size reduced-section transverse tensile specimen with a 3 mm gauge length, a 3 mm width in gauge length, and a 2 mm thickness. The full-length tensile specimen was used to determine the strength and weakest region of the weldment. In the reduced-section tensile specimen, the cross-section area in the region was intentionally reduced to determine the strength of the dissimilar weld. These tensile specimens were cut using precision wire-EDM from the as-received and dissimilar welded samples. Following the ASTM E-8 (M) standard, different strain rates were used for full-length and reduced-

section tensile specimens [116]. The strain rate of 1 mm/min for the full-length specimen and 0.5 mm/min for the reduced section tensile specimen was selected. Fractured samples were analysed under high-resolution field emission scanning electron microscopy (FESEM).

3.8.8 Charpy impact testing

The Charpy impact test is a widely used method to determine the toughness or impact resistance of materials, especially metals. It provides necessary information about a material's ability to absorb energy under sudden, dynamic loading conditions. This is a critical test for evaluating the behaviour of materials under sudden or impact loading. It is particularly important in industries where the unexpected impact is a potential risk to the structural integrity and safety of components and structures. Sometimes ductile materials fail like brittle materials under sudden or impact loading, and it is further increased when there is any notch present in the ductile materials. This catastrophic brittle failure could be reduced when high-toughness material is used.

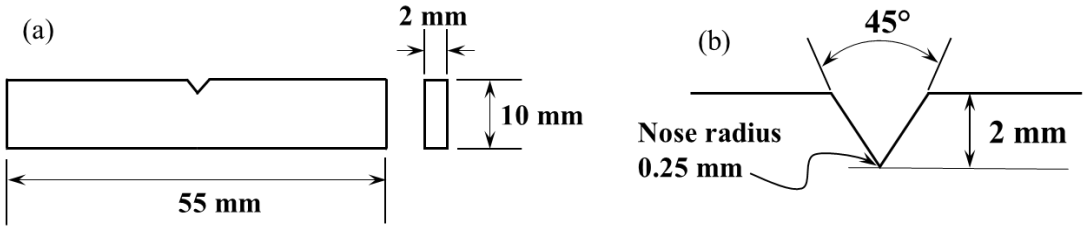

Figure 3.19 (a) Sub-size impact test specimen; (b) details of notch in the specimen

Here, welded specimens with a notch at the center were tested as per Section A3 of the ASTM standard E23-07a. The sub-size Charpy impact test specimen with dimensions of 55 mm long, 10 mm wide, 2 mm thick, and a notch at the center is shown in Figure 3.19 (a). Figure 3.19 (b) shows the detailing (45° and 2 mm deep) about the notch created in the specimen. Specimens from the weldment and as-

received specimens were extracted using precision wire-cut EDM, and an accurate notch was created using a specially designed motorized broaching machine (Model: BMF-M). Charpy impact testing was performed with two schemes, initially, a notch was created at the weld center with varying frequency to determine the impact strength of the weld, and later, a notch was created in the different zones (weld, HAZ of the CP-Ti side, and HAZ of Ti-6Al-4V) of the welds of conventional and pulsed GTAW dissimilar titanium welds. Charpy tests were performed on a motorized digital computerized Charpy pendulum impact machine (Model No. A/T ISO-ASTM/ISO(D)).

3.8.9 Impression creep testing

Generally, impression creep testing is a fast technique and could be performed in the very narrow region such as HAZ and weld region of the weldment to investigate the creep behaviour of that region. Due to the very narrow zone with limited testing area, conventional creep testing methods would be extremely difficult to obtain zone-wise creep behaviour of weldments. In order to address this issue, Impression creep testing could be employed for understanding the steady state creep behaviour, determining the activation energy, and determining the governing creep mechanism from the stress exponent. For the detailed discussion regarding understanding of impression creep technique refer to Section 2.6.

Analysis of impression creep parameters

In the impression creep testing method, a flat cylindrical indenter with a diameter of *'d'* applies a constant load *'L'* on the specimen surface. The following relationships are used to analyse impression creep.

$$\sigma_{imp} = \frac{4L}{\pi d^2} \qquad \text{Eq. 3.1}$$

$$v_{imp} = \frac{dh}{dt} \qquad \text{Eq. 3.2}$$

Equation 3.1 helps in determining the punching or impression stress below the indenter, denoted as *'σ_{imp}',* and equation 3.2 helps in determining the penetration rate or impression velocity of the indenter, denoted as *'v_{imp}'.* Where *'dh'* denotes the depth of penetration in time *'dt'*.

Correlation between impression creep and uniaxial creep

The impression creep data can be more useful if it can be co-related with conventional tensile creep testing. The relationship between impression creep parameters (σ_{imp} and v_{imp}) and uniaxial tensile creep parameters (σ_{uni} and $\dot{\varepsilon}_{uni}$) has been established by the various researchers [101, 117, 118]. Where steady state creep rate ($\dot{\varepsilon}_{uni}$) during tensile creep testing is directly proportional to the ratio of steady state impression creep velocity (v_{imp}) to the indenter diameter *'d'* and can be represented as equation 3.3,

$$\dot{\varepsilon}_{uni} = \frac{v_{\text{imp}}}{\beta d} \qquad \textit{Eq.}3.3$$

where β is the co-relation factor.

Similarly, correlations between equivalent uniaxial stress (σ_{uni}) and punching stress (σ_{imp}) were deduced empirically and can be written as equation 3.4 using the correlation factor α,

$$\sigma_{uni} = \alpha\sigma_{\text{imp}} \qquad \textit{Eq.}\ 3.4$$

The stress correlation factor α is equivalent to the constraint factor, which relates the hardness and uniaxial flow stress of the materials [119].

The creep rate dependence on temperature in conventional tensile creep analysis at constant stress follows the Arrhenius type power-law relationship represented by

equation 3.5,

$$\dot{\varepsilon}_{uni} = A\sigma_{uni}^{n}\exp\left(Q_C/RT\right) \quad , \qquad \text{Eq. 3.5}$$

where A is a constant, Q_c is activation energy, and n is the stress exponent.

In case of impression technique, equations 3.5 can be modified by substituting the conventional tensile creep parameters by impression creep parameters from equation 3.3 and 3.4 in equation 3.5.

$$\frac{v_{imp}}{d} = A\sigma_{imp}^{n}\exp\left(Q_C/RT\right) \qquad \text{Eq. 3.6}$$

Equation 3.6 represents the Arrhenius power-law relationship for the impression creep test, and using this equation, the value of activation energy and stress exponent were calculated.

The correlation factor 'β' in equation 3.3 and the stress correlation factor 'α' in equation 3.4 were taken from literature and can be used to convert the data from the impression creep test to the equivalent tensile creep test data in the steady state region. Therefore, in order to estimate the activation energy and stress exponent through impression creep testing, the values of α and β were taken as 0.3 and 1, respectively.

Metallographic sample preparation and impression creep testing

Samples of welded sheet (depicted in Figure 3.14 (c-d)) were used for metallographic examination and impression creep testing. Before impression creep testing, the metallographic studies of different regions of weldment were performed under an optical microscope. Metallographic samples for microscopy were prepared and etched the same as those prepared for optical microscopy of the welded specimen. Figure 3.20 (a) shows the impression creep testing set-up along with its assembly. Figure 3.20 (b) shows the tungsten carbide flat-end cylindrical indenter of 1 mm

diameter, which was used for indentation. Samples for impression creep tests were extracted using precision wire-cut EDM from the different zones of the weldment. The extracted samples were flattened using coarse grade emery paper and then polished and etched to reveal the different regions. Figure 3.20 (c) shows samples of different regions for impression creep testing. This helped in identifying the precise location of different zones for indentation. Figure 3.20 (c-i) shows the polished and etched samples before impression creep testing, and Figure 3.20 (c-ii) shows the samples after impression testing. The impression creep tests were performed in a high vacuum (2×10^{-6} mbar) chamber. This was essential to avoid any oxidation during impression creep testing.

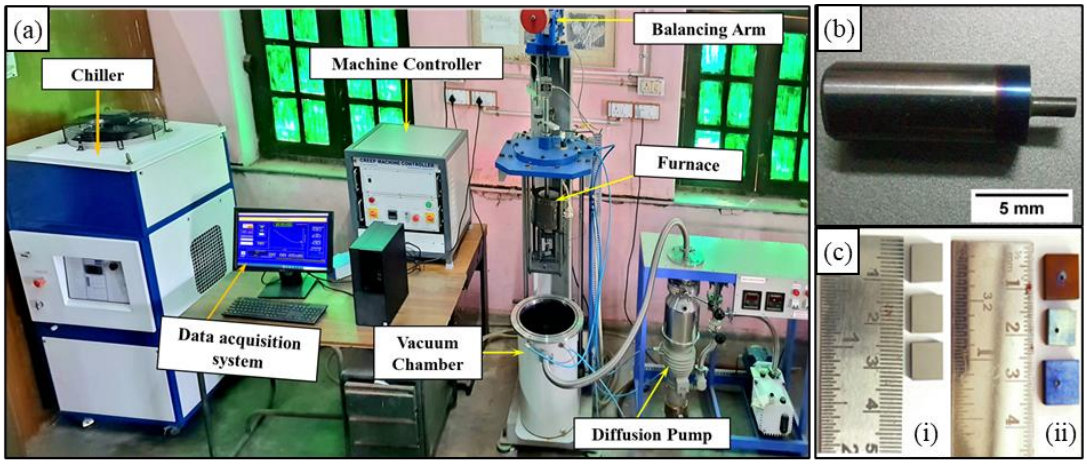

Figure 3.20 (a) Impression creep testing set-up; (b) indenter with 1 mm diameter pin; (c) (i) samples before impression creep testing, (ii) samples after impression creep testing

A linear variable differential transformer (LVDT) was employed for measuring the impression depth with a linear error of ±0.5%. The impression depth with respect to time was recorded using a data acquisition system. Impression creep-tested samples were cut cross-sectionally and polished in order to examine the microstructure variations that appeared during testing. Optical microscopy of crept specimens was carried out to study the microstructure evolution during creep. The distinct microstructural features that appeared after the impression creep test were used to

observe the corelation of possible creep mechanisms predicted by the empirical models. The samples for metallographic studies were prepared in the same way as those prepared for optical microscopy, and the samples were analysed under a Leica DFC295 metallurgical microscope.

Table 3.7 Impression creep testing conditions for base, HAZ and weld region

Region of weldment	Temperatures (K)	Stresses (MPa)
Base (CP-Ti)	773	500
	793	500
	813	500
	793	480
	793	460
HAZ (CP-Ti)	773	500
	793	500
	813	500
	793	480
	793	460
Dissimilar weld (CP-Ti/Ti-6Al-4V)	848	900
	873	900
	898	900
	898	850
	898	800
HAZ (Ti-6Al-4V)	873	1110
	923	1110
	898	1110
	898	1060
	898	1160
Base (Ti-6Al4V)	848	900
	873	900
	898	900
	898	850
	898	800

The impression creep testing conditions in terms of stress and temperature for each region are listed in Table 3.7. The stresses temperature imposed for impression creep testing were selected depending on the maximum stresses reached during possible

high temperature application of titanium alloys. Titanium alloys are mostly used in high temperature applications in gas turbines, where the maximum stress reaches around 1000 MPa and the temperature is around 600°C [120]. Another criterion used for the selection of stress was that the stress values prevailing during testing was such that the test could be completed in a reasonable time. This was particularly important because generally titanium alloys have a very good creep resistance and show very exhaustive creep resistance at lower stresses. Therefore, the stresses were selected around the maximum application stress, and at these stresses, tests ran for a sufficiently long time so that reliable results could be obtained. Along with the range of stress and temperature, the test matrix was designed in such a way that a minimum number of tests should be required to determine the activation energy and stress exponent.